

Gutzwiller Magnetic Phase Diagram of the Cuprates

R.S. Markiewicz,^{1,2,3} J. Lorenzana,^{2,3} G. Seibold,⁴ and A. Bansil¹

¹ *Physics Department, Northeastern University, Boston MA 02115, USA*

² *SMC-INFM-CNR and Dipartimento di Fisica, Università di Roma “La Sapienza”, P. Aldo Moro 2, 00185 Roma, Italy*

³ *ISC-CNR, Via dei Taurini 19, I-00185 Roma, Italy*

⁴ *Institut Für Physik, BTU Cottbus, PBox 101344, 03013 Cottbus, Germany*

A general constructive procedure is presented for analyzing magnetic instabilities in two-dimensional materials, in terms of [predominantly] double nesting, and applied to Hartree-Fock HF+RPA and Gutzwiller approximation GA+RPA calculations of the Hubbard model. Applied to the cuprates, it is found that competing magnetic interactions are present only for hole doping, between half filling and the Van Hove singularity. While HF+RPA instabilities are present at all dopings (for sufficiently large Hubbard U), in a Gutzwiller approximation they are restricted to a doping range close to the range of relevance for the physical cuprates. The same model would hold for charge instabilities, except that the interaction is more likely to be q -dependent.

PACS numbers:

I. INTRODUCTION

The charge and magnetic instabilities of one dimensional materials are well understood in terms of Fermi surface (FS) nesting. Here it is shown that for two-dimensional materials, features in maps of the bare susceptibility can be understood in terms of a series of FS ‘nesting curves’, and the dominant instabilities are generally related to *double nesting* features. The analysis shows how to locate these nesting features in momentum (\mathbf{q}) space, often providing analytical expressions. As an application, the full evolution with doping of the leading magnetic instabilities for several families of cuprates is presented, both in the conventional Hartree-Fock (HF) plus RPA (HF+RPA) and in a Gutzwiller approximation (GA+RPA) calculation. The analysis provides a pseudogap candidate and makes the surprising prediction that the ‘checkerboards’ seen in scanning tunneling microscopy (STM) studies are *not* the same phase as the ‘stripes’ in $\text{La}_{2-x}\text{Sr}_x\text{CuO}_4$ (LSCO).

The present results should find extensive utilization. First, for weakly correlated two-dimensional systems the HF+RPA results provide an essentially complete solution to the nesting problem, as long as the interaction U is \mathbf{q} -independent. The GA+RPA extends the results into the intermediate coupling regime. In both cases, the magnetic instabilities are determined by zeroes of the Stoner denominator,

$$1 - U_{eff}\chi_0(\mathbf{q}, \omega = 0). \quad (1)$$

Here for cuprates U_{eff} is the Hubbard U in HF+RPA, and a more complicated \mathbf{q} -dependent object $U_{GA}(\mathbf{q})$ in the GA+RPA calculation. Thus, the leading HF+RPA instability is simply associated with the maximum of the bare susceptibility $\chi_{0M} = \max_{\mathbf{q}} \chi_0(\mathbf{q}, 0)$, while the leading Gutzwiller instability can be shifted by the \mathbf{q} -dependence of $U_{GA}(\mathbf{q})$. It will be clear that the same analysis can be extended to any two-dimensional material.

The cuprates appear to be in an intermediate coupling regime where the Gutzwiller results can be expected to provide a good approximation to the phase diagram at $T = 0$. Thus, in the cuprates, recent quantum Monte Carlo (QMC)¹ and ‘quasiparticle-GW’ (QP-GW)² calculations have been able to reproduce experimental ARPES spectra of optimally and overdoped cuprates, starting essentially from LDA bands and calculating the self-energy self consistently. In the QP-GW approach, the self energy is calculated as a convolution over a renormalized RPA susceptibility. Not only is the low-energy dispersion renormalization reproduced, but also the ‘waterfall’ effect³, which represents the dressing of low-energy quasiparticles by (mainly) spin fluctuations. Extension of these results to the hole-underdoped regime will require identification of the phase or phases responsible for the pseudogap. Since these are most likely to be incommensurate density wave or ‘stripe’ phases, the QMC calculations have a severe problem of limited \mathbf{q} -resolution, while the QP-GW calculations are ideally suited to handle this. Such an approach has had considerable success with electron-doped cuprates, where the leading instability is commensurate (π, π) . (We set the lattice constant $a \equiv 1$.)

The paper is organized around the Stoner criterion as follows. Sections 2-3 describe the calculations of the zero frequency bare susceptibility $\chi_0(\mathbf{q})$, and determining its maximum χ_{0M} . In Section 2 we introduce the concept of nesting curve, associated with the nesting criterion $\mathbf{q} = 2\mathbf{k}_F$, where \mathbf{k}_F is the (anisotropic) Fermi wave vector, and we demonstrate that χ_{0M} is generally associated with a double nesting. We apply this concept to the cuprates, taking the hopping parameters from tight-binding one-band fits to the LDA dispersions, and show that over most of the doping range there is a unique χ_{0M} , with a surprising electron-hole symmetry. In Section 3 we extend this analysis to the more complicated hole doping regime for doping x between half filled and the doping of the Van Hove singularity (VHS). Here competing magnetic phases are found, and

the dominant phase is sensitive to material parameters, being different for different cuprates. Section 4 describes the GA+RPA technique and introduces the corresponding $U_{eff} = U_{GA}(\mathbf{q})$. Section 5 presents the resulting Gutzwiller magnetic phase diagrams. It is found that the phase diagram of $\text{La}_{2-x}\text{Sr}_x\text{CuO}_4$ (LSCO) is distinct from that of most other cuprates, but that for all cuprates, using a bare Hubbard $U = 8t$, the paramagnetic state is unstable at the GA level for all relevant dopings, including the overdoped regime. A discussion is presented in Section 6, and conclusions in Section 7.

II. SUSCEPTIBILITY PLATEAUS

The present calculations are based on tight-binding parametrizations of typical dispersions for single-layer cuprates, including models of $\text{La}_{2-x}\text{Sr}_x\text{CuO}_4$ (LSCO), $\text{Nd}_{2-x}\text{Ce}_x\text{CuO}_4$ (NCCO), and $\text{Bi}_2\text{Sr}_2\text{Cu}_1\text{O}_6$ (Bi2201), Table I in Appendix A. For NCCO, Bi-2201(2), and LSCO(2), the parameters are based on a tight-binding fit to the LDA bands⁴, while sets Bi-2201(1) and LSCO(1) are direct fits to the experimental bands. In all cases, k_z dispersion is neglected, approximating the cuprates as two-dimensional.

The real part of the susceptibility $\chi'_0(\mathbf{q}, \omega = 0)$ is dominated by a series of plateaus, with the largest susceptibility systematically shifting from one plateau to another as a function of doping. Figure 1 shows that these and related features dominate χ'_0 over the full doping range, and further reveals a striking quasi-electron-hole symmetry of the evolution. However, instead of being symmetric about $x = 0$, the evolution is symmetric about the doping of the Van Hove singularity (VHS), x_{VHS} , where the Fermi energy coincides with the VHS, $E_F = E_{VHS}$, and the density of states (DOS) diverges logarithmically. Figure 1(a) shows χ'_0 calculated along the high symmetry axes of LSCO, for the full electron-doping range $n = 1 - x$ from 1 to 2, with an extension to the hole doping of the VHS (blue curves). Near half filling the susceptibility is dominated by the well-known plateau⁵ near (π, π) (red and blue curves), which peaks at the VHS. As electron-doping increases, the peak shifts to a second plateau near $(\pi, 0)$ (green curves), then to a third near Γ for a nearly full band (brown curves). The *same* sequence is followed for hole doping, Fig. 1(b).

In addition to these plateaus, there is an additional Γ -centered feature, which is prominent near the doping of the VHS, but has largely disappeared by half filling. This feature will be referred to as the antinodal nesting (ANN) plateau. Bi2201 displays the same plateaus, with the same quasi-electron-hole symmetry, Fig. 1(c,d). A key difference is that the (π, π) -plateau of Bi2201 is convex over a considerably wider doping range than in LSCO, before turning concave near the VHS. This has a consequence that the ANN peak dominates over a wide doping range in Bi2201, but only in the immediate vicinity of the VHS in LSCO. At the VHS, the bare susceptibility di-

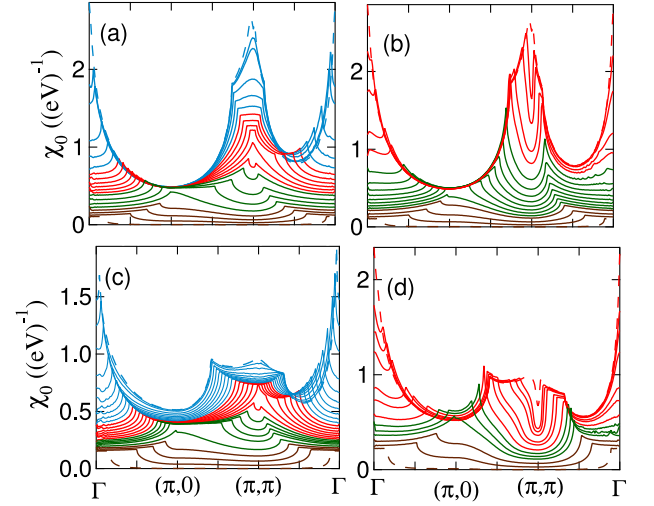


FIG. 1: (Color online.) (a) Susceptibility $\chi'_0(\omega = 0)$ for LSCO as a function of \mathbf{q} for a series of dopings from $x_{VHS} = 0.207$ (blue dashed line) to $x = -0.99$ (brown dashed line). [Blue curves are for hole doping, $x > 0$, others for electron doping, $x \leq 0$.] Note the evolution from a plateau near (π, π) (blue and red lines) to one near $(\pi, 0)$ (green) to one near Γ (brown). Band parameters appropriate to LSCO(2) (Table I). (b) Same as (a), except for hole dopings $x = 0.207$ (red dashed line) to $x = -0.99$ (brown dashed line). Note similar evolution of plateaus. (c,d) Similar to (a,b), except for Bi-2201 (2 in Table I). Note overall similarity, except for curvature near (π, π) . Dashed curves correspond to $x =$ (c): -0.99 (brown) or 0.43 (blue); (d): 0.44 (red) or 0.99 (brown). Curves are generally spaced by $\Delta x = 0.05$, except for (1) higher density near points of rapid change (e.g., the VHS), (2) $\Delta x = 0.1$ near top and bottom of band, and (3) end points at $x = \pm 0.99$.

verges logarithmically both at Γ (where it is equal to the DOS) and at (π, π) , but the latter divergence is quite weak and not apparent in the numerical calculations of Fig. 1. Despite the apparent complexity of these evolving susceptibility patterns, the plateau evolution can be understood in detail, with analytic formulas for the positions of all dominant peaks.

The generic evolution of the plateaus from $(\pi, \pi) \rightarrow (\pi, 0) \rightarrow (0, 0)$ can be understood with reference to the ‘nesting curves’, Fig. 2. For the generic case of two Fermi surface segments, a nesting curve can be defined as the locus of all points $\mathbf{q} = \mathbf{k}_{F1} - \mathbf{k}_{F2}$, where \mathbf{k}_{Fi} is a point on the i th FS, FS_i , with the restriction that when FS_1 is shifted by \mathbf{q} it is tangent to FS_2 . For the cuprates, there is usually just a single FS section [an exception is given below in Section III, Fig. 6], and the nesting curves simplify to plots of

$$\mathbf{q} = 2\mathbf{k}_F, \quad (2)$$

for any Fermi momentum \mathbf{k}_F , Fig. 2. Since the point (π, π) lies on horizontal and vertical planes of reflection symmetry for the susceptibility, the nesting curves must be supplemented by their reflections about the lines

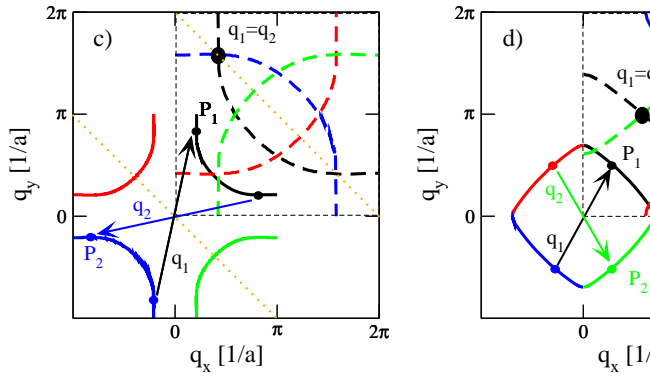
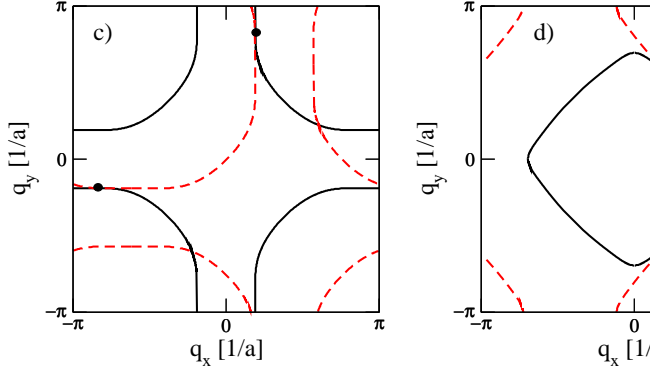


FIG. 2: (Color online.) (a) Hole-like Fermi surface (solid) shifted by the double nesting vector $\mathbf{q} = (0.38, 1.62)\pi/a$ and folded back into the first BZ (dashed). (b) Electron-like Fermi surface (solid) shifted by the double nesting vector $\mathbf{q} = (0.58, 1)\pi/a$ and folded back into the first BZ (dashed).

$q_x = \pi, q_y = \pi$. Fig. 3 shows three sets of nesting curves corresponding to three hole dopings for LSCO (dispersion 1), $x = 0.41$ (red curves), 0.62 (blue), and 0.79 (green). Frames (b-d) show the corresponding susceptibility maps $\chi'_0(\mathbf{q})$, and it can be seen that the ridges in χ'_0 are exactly given by the nesting curves. [For convenience, the $x = 0.41$ data is replotted in Fig. 3(a). Note that the susceptibility maps are plotted over the range of q_x, q_y between 0 and π , whereas the nesting curves are plotted over the wider range 0 to 2π .] Furthermore, the dominant peaks in χ'_0 correspond to the intersection of two nesting curves. By drawing the original and \mathbf{q} -shifted Fermi surfaces (FSs), Figs. 2(a), (b), it can be seen that this overlap corresponds to the simultaneous nesting of two different sections of FS. Hence the term ‘double nesting’.

As shown in Figs. 2(c), (d) this kind of ‘double nesting’ can originate from either the scattering between points on opposite segments (cf. example in Fig. 2(c)) or adjacent segments (cf. example in Fig. 2(d)) of the FS. In the example shown in Fig. 2(c) we denote the scattered states on the FS as $\mathbf{P}_1 = (\delta_\perp, \pi - \delta_\parallel)$ and $\mathbf{P}_2 = (-\pi + \delta_\parallel, -\delta_\perp)$ which yield the points on the nesting curves $\mathbf{q}_1 = 2\mathbf{P}_1 = (2\delta_\perp, 2\pi - 2\delta_\parallel) \equiv (2\delta_\perp, -2\delta_\parallel)$ and $\mathbf{q}_2 = 2\mathbf{P}_2 = (-2\pi + 2\delta_\parallel, -2\delta_\perp) \equiv (2\delta_\parallel, -2\delta_\perp)$. Thus in this case ‘double nesting’ ($\mathbf{q}_1 = \mathbf{q}_2$) occurs when $\delta_\perp = \delta_\parallel$ which generally can only be fulfilled for points near the antinodes of hole-like FS’s. These are thus referred to as antinodal nesting (ANN) features. More common is the situation sketched in Fig. 2(d) where we consider the scattered states $\mathbf{P}_1 = (\delta_\perp, \pi - \delta_\parallel)$ and $\mathbf{P}_2 = (\delta_\perp, -\pi + \delta_\parallel)$. In this case the ‘double nesting’ condition $\mathbf{q}_1 = \mathbf{q}_2$ can only be fulfilled for $\delta_\parallel = 0$ (which is trivial since initial and final states of the two scattering processes are identical) or $\delta_\parallel = \pi/2$. The latter condition implies that this kind of ‘double nesting’ generally affects the nodal states and leads to scattering vectors \mathbf{q} close to $(\pi/a, \pi/a)$, generating the (π, π) -plateau.

A slightly different point of view might help clarify the role of double nesting. Tangency of two Fermi surface segments [‘nesting’] means a stability of FS overlap, in that the nesting persists if one displaces the nesting vector in a particular direction. Then double nesting means tangency along two surface segments, so nesting persists if one displaces the nesting vector in two (rather than one) directions.

The origin of the plateau transitions is now apparent: as hole doping increases, the FS shrinks to a small pocket near Γ before disappearing. The nesting curves shrink in a similar fashion, but with a doubled radius, since $\mathbf{q} = 2\mathbf{k}_F$. Thus the dominant overlap shifts from near (π, π) at the VHS (Fig. 2(b)) towards $(\pi, 0)$ (Fig. 2(c)), and finally towards Γ , in Fig. 2(d), thereby explaining the plateau evolution. For electron doping, the Fermi surface ultimately closes at (π, π) , leading to the same sequence of plateau transitions, as illustrated in Fig. 4, where the nesting maps are directly superposed on the susceptibility curves. In the doping range relevant to the cuprates, the physics of NCCO is dominated by the (π, π)

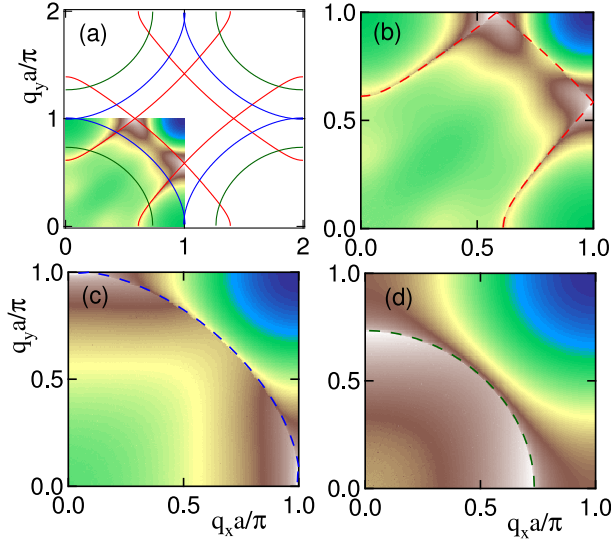


FIG. 3: (Color online.) (a) Nesting maps $q = 2k_F$ for LSCO, dispersion 1, and $x = 0.41$ (red curves), 0.62 (blue), and 0.79 (green). Corresponding susceptibility $\chi'_0(\omega = 0)$ as a function of q for a series of hole dopings from $E_F[x] = -0.16$ [0.41] (b), -0.3 [0.62] (c), and -0.5 eV [0.79] (d). In all figures, whites are largest χ s, blues are smallest.

plateau, Fig. 4a and red curves in Fig. 1(a), which shrinks to a point at the end of the ‘hot-spot’ regime.

In all cases, the dominant peak lies along a high symmetry axis, and the doping dependence of its position can readily be found from the dispersion

$$E(\mathbf{k}) = -2t[c_x(a) + c_y(a)] - 4t'c_x(a)c_y(a) - 2t''[c_x(2a) + c_y(2a)] - 4t'''[c_x(2a)c_y(a) + c_y(2a)c_x(a)], \quad (3)$$

where

$$c_i(\alpha a) \equiv \cos(\alpha k_i a), \quad (4)$$

and α is an integer (or half-integer). For this dispersion, the VHS is generally at $(\pi, 0)$, or $E_{VHS} = 4t' - 2t''$. The positions of the peaks in Fig. 3(b,c) and Fig. 4(b,c) lie along the zone boundary ($q_x a = \pi$) with

$$q_y a = 2 \arccos[\pm \sqrt{b^2 - c} - b], \quad (5)$$

with $b = (t - 2t''')/[4t'']$ and $c = [E_F - 4t'']/[4t'']$. For electron [hole] doping the peak is exactly at $(\pi, 0)$ when $E_F = +[-]2(t - 2t''')$. Beyond this point, the peak is at $q_y = 0$, q_x given by Eq. 5 with $b = (t - [+]2t' + 2t''')/[4(t'' - [+]2t''')]$ and $c = [E_F - [+]2(t - 2t''')]/[4(t'' - [+]2t''')]$. Since a peak at Γ corresponds to ferromagnetism, the above reproduces the common finding that a nearly empty or nearly full band tends to be ferromagnetic. The ANN peak $\mathbf{q}_1 = \mathbf{q}_2$ in Fig. 2a satisfies $\cos(q_y a) = [E_F - 2t']/[2(t' - 2t'')]$. Thus the peak susceptibility is generally associated with double nesting.

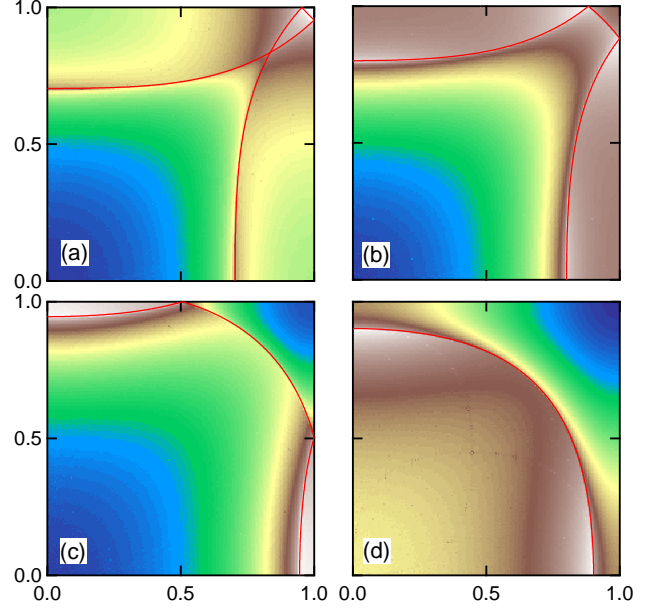


FIG. 4: (Color online.) Susceptibility $\chi'_0(\omega = 0)$ as a function of q with superposed nesting maps $q = 2k_F$ for NCCO, for a series of electron dopings ($x < 0$) from $x[E_F] = -0.26$ [0.10] (a), -0.37 [0.20] (b), -0.52 [0.35] (c), and -0.65 [0.50 eV] (d).

The only exception we have found to this is a tendency to remain commensurate for a finite doping range about high symmetry points such as (π, π) or $\Gamma = (0, 0)$,⁶ – a form of Van Hove nesting⁷.

III. COMPETING PHASES AND FERROMAGNETISM

While the above sequence is completely generic, holding for all cuprates and being electron-hole symmetric, the additional features associated with the VHS are considerably more variable. Fig. 5 illustrates the low-hole doping regime for three dispersions proposed for the cuprates. At half filling, all three have a peak susceptibility on the (π, π) plateau, associated with conventional staggered antiferromagnetism (SAF). At low doping the peak is either commensurate or $(\pi, \pi - \delta)$ incommensurate, with δ increasing with doping. For finite hole doping a new feature emerges, a roughly + - shaped peak along the zone diagonal, at $(\pi - \delta, \pi - \delta)$. From the nesting curves, it can be seen that the peak is associated with nesting of the flat sections of the bands near $(\pi, 0)$ – hence the name antinodal nesting (ANN) – but the largest susceptibility lies along the zone diagonal, where both $(\pi, 0)$ and $(0, \pi)$ nesting occur simultaneously, Fig. 2a. This ANN feature has an interesting relation with ‘hot spot’ physics⁸. A ‘hot spot’ is a point of the Fermi surface which is simultaneously on the antiferromagnetic (AF) zone boundary [diagonal of the paramagnetic Brillouin zone]. From Fig. 2(c) it becomes apparent (cf. large

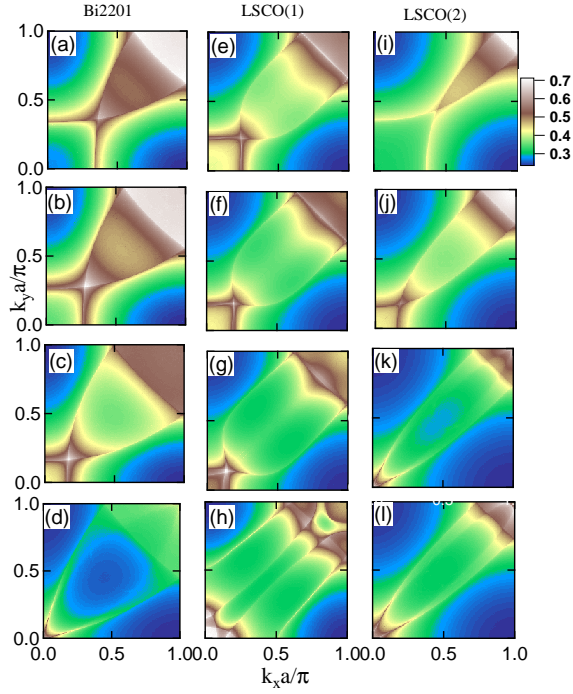


FIG. 5: (Color online.) Susceptibility maps for Bi2201 (a-d), LSCO(1) (e-h), and LSCO(2) (i-l) at a series of increasing dopings. $x [E_F] = 0.12 [-0.20]$ (a), $0.20 [-0.25]$ (b), $0.31 [-0.30]$ (c), $0.40 \simeq x_{VHS} [0.33]$ (d); $0.19 [-0.12]$ (e), $0.23 [-0.13]$ (f), $0.29 [-0.14]$ (g), $(x_{VHS} \simeq 0.33)$, $0.37 [-0.15]$ (h); $0.0 [-0.05]$ (i), $0.14 [-0.10]$ (j), $0.20 \simeq x_{VHS} [-0.111]$ (k), and $0.21 [-0.1112 \text{ eV}]$ (l).

dot) that the image of the AF zone boundary in the extended \mathbf{q} -map intersects the ‘nesting curves’ exactly at the points of ‘double nesting’. But the image of the AF zone boundary gets folded in the \mathbf{q} -map onto the zone diagonal, $\Gamma \rightarrow (\pi, \pi)$, thereby generating the usual ANN feature. Thus all the diagonal ANN peaks in \mathbf{q} arise from hot spots in k . As the doping of the VHS is approached the hot spots move toward $(\pi, 0)$ and the nesting curve moves to Γ . Since the susceptibility at Γ is equal to the DOS, it diverges at the VHS, thereby controlling the magnetic instability.

The appearance of the ANN peak leads to a competition between two different kinds of magnetic order, and the doping evolution of the susceptibility maps diverges. For most dispersions studied, including the left and central columns of Fig. 5, the ANN intensity grows and the dominant peak changes discontinuously from the SAF plateau to ANN nesting. For the Bi-2201 dispersion (left column) this ANN peak becomes dominant at about $x=0.2$, and evolves smoothly to Γ at $x=0.4$. If one unfolds the nesting curve, one sees that this happens exactly at the doping of the VHS, when the FS passes through $(\pi, 0)$. The central column, corresponding to an extreme dispersion proposed for LSCO to enhance antinodal nesting, displays a much more complicated nesting

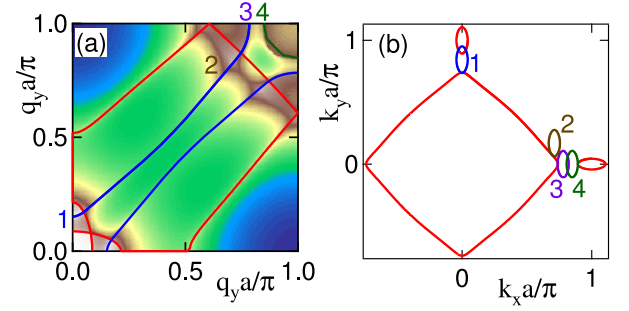


FIG. 6: (Color online.) (a) Susceptibility map for LSCO(1) (h) with nesting curves superposed. Red curves: $\mathbf{q} = 2\mathbf{k}_F$ nesting for both Γ -centered barrel and $(\pi, 0)$, $(0, \pi)$ -centered pockets. Blue lines = barrel-pocket nesting; green line = inter-pocket nesting. (b) Corresponding Fermi surface map showing four \mathbf{q} -shifted pockets, labelled as in (a).

map over a limited doping range close to the VHS, but also displays a dominant peak at Γ exactly at the VHS. This map will be explained below. Finally, for the right column, corresponding to a more conventional dispersion for LSCO, the ANN peak is weaker than the SAF peak except in the immediate vicinity of the VHS. In this case, the dominant susceptibility peak remains commensurate at (π, π) until the doping of the VHS, jumps to Γ at the VHS, then jumps back and smoothly evolves to $(\pi, \pi - \delta)$ incommensurate [this sequence can also be followed in Fig. 1(a),(b)]. Note further, in Fig. 5(i,j), that there is a wide doping range where the susceptibility peak remains commensurate, at (π, π) . [Since (π, π) lies along several mirror planes, the corresponding susceptibility is in general a local maximum or minimum.]

The complicated nesting map of the middle column near the VHS is explained in Fig. 6. The dispersion is such as to produce an ‘extended VHS’,⁹ which first intersects the $\Gamma \rightarrow (\pi, 0)$ axis at a point $(\pi - \delta, 0)$. For larger hole doping, the FS has two sheets, one a squarish barrel centered at Γ , the other a pocket centered at $(\pi, 0)$, Fig. 6(b). The intrasheet $\mathbf{q} = 2\mathbf{k}_F$ nesting maps are shown by the red curves in Fig. 6(a). In addition to the one associated with the barrel FS, there are two overlapping segments associated with the pockets, but translated by the \mathbf{q} folding to the vicinity of Γ . As in the other frames of Figs. 2-4, these nesting curves exactly match some of the ridges seen in the susceptibility. However, there are additional ridges, associated with nesting between two different FS segments. Thus, the blue curves in Fig. 6(a) represent barrel-pocket nesting – that is, the locus of the \mathbf{q} -vectors needed to shift the pocket until it is tangent to some point on the barrel FS. For instance, the points labelled 1, 2, 3 represent translations equivalent to those shown in Fig. 6(b). The new nesting curves can easily be found numerically, by requiring that the two FS sections have a common tangent at the point of osculation. Similarly, the green curve near (π, π) represents

inter-pocket nesting, with point 4 illustrating one particular nesting vector. It can be seen that the full collection of nesting curves explains all of the ridge-like features seen in the susceptibility map, and in particular allow the determination of the points of maximal susceptibility, except for the above-noted commensurability effects. Note however, that despite these complications, the susceptibility peak moves to Γ in a finite doping range about the point where the antinodal electron pocket shrinks to zero width.

The above discussion can be summarized: in the doping between half filling and the VHS, a new susceptibility peak arises, associated with nesting of the antinodal parts of the large FS. Two kinds of behavior are found: when the ANN is dominant, the peak evolves to Γ at the VHS. On the other hand, for LSCO(2) with small t' , the ANN peak is inherently weaker than the (π, π) peak, in which case the susceptibility remains commensurate at (π, π) from half filling almost to the VHS, then smoothly develops a $(\pi, \pi - \delta)$ incommensurability. Yet even here, in the immediate vicinity of the VHS, the ANN peak at Γ becomes dominant in a very limited doping range. Hence, for most dispersions the susceptibility will have strong FM fluctuations near the VHS, while for other dispersions the fluctuations remain mostly AFM.

IV. GUTZWILLER CALCULATION AND U_{eff}

In the GA+RPA calculation^{10,11}, the electronic paramagnetic ground state energy is calculated in the GA^{13,14} and then expanded to second order in the on-site and intersite magnetic fluctuations in the spirit of Vollhardt's Fermi liquid approach¹⁵. Response functions are computed using linear response in the presence of small external field.¹⁰ One obtains RPA like susceptibilities but with strong vertex corrections. As shown in Appendix B longitudinal and transverse susceptibilities are trivially related and lead to the same Stoner criteria as required by spin rotational invariance. In terms of a tensor bare transverse susceptibility (cf. Appendix B and Appendix C)

$$\begin{aligned} \chi_{0\mathbf{q}} &= \begin{pmatrix} \chi_{11}^0 & \chi_{12}^0 \\ \chi_{21}^0 & \chi_{22}^0 \end{pmatrix} \\ &= \frac{1}{N} \sum_{\mathbf{k}} \begin{pmatrix} 1 & E_{\mathbf{k},\mathbf{q}} \\ E_{\mathbf{k},\mathbf{q}} & E_{\mathbf{k},\mathbf{q}}^2 \end{pmatrix} \frac{n_{\mathbf{k}+\mathbf{q}} - n_{\mathbf{k}}}{\epsilon_{\mathbf{k}+\mathbf{q}} - \epsilon_{\mathbf{k}}}, \end{aligned} \quad (6)$$

with $E_{\mathbf{k},\mathbf{q}} = \epsilon_{\mathbf{k}+\mathbf{q}}^0 - \epsilon_{\mathbf{k}}^0$, the GA+RPA dressed susceptibility $\chi_{\mathbf{q}}$ is given by

$$\chi_{\mathbf{q}}^{-1} = \chi_{0\mathbf{q}}^{-1} - V_{\mathbf{q}}^{+-}. \quad (7)$$

Here the ratio of dressed to bare dispersion is given by $\epsilon_{\mathbf{k}}/\epsilon_{\mathbf{k}}^0 = Z$, with the Gutzwiller renormalization factor

$$Z = z_0^2 = 4 \frac{\left[\sqrt{(x+D)(\frac{1-x}{2}-D)} + \sqrt{D(\frac{1-x}{2}-D)} \right]^2}{1-x^2} \quad (8)$$

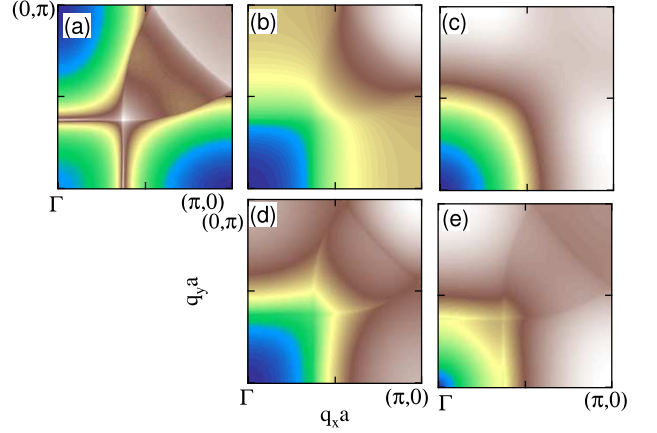


FIG. 7: (Color online.) Susceptibility maps (a) χ_{11}^0 , (b) χ_{12}^0 , and (c) χ_{22}^0 , along with derived quantities (d) \bar{E}_1 and (e) \bar{E}_2 , as a function of \mathbf{q} for Bi2201 with $x = 0.15$.

which depends on the GA double occupancy variational parameter D and the doping x . The interaction matrix is¹⁰

$$V_{\mathbf{q}}^{+-} = \begin{pmatrix} N_{\mathbf{q}} & M_{\mathbf{q}} \\ M_{\mathbf{q}} & 0 \end{pmatrix}, \quad (9)$$

which is defined in Appendix B.

While Eq. 7 is a tensor equation, it can be expanded into the form of Eq. 1 with $\chi_0 = z_0^2 \chi_{11}^0$ and $U_{eff} = U_{GA}$,

$$U_{GA} = (N_{\mathbf{q}} + 2M_{\mathbf{q}}\bar{E}_1 + M_{\mathbf{q}}^2(\bar{E}_2^2 - \bar{E}_1^2)\chi_0/z_0^2)/z_0^2, \quad (10)$$

with $\bar{E}_1 = \chi_{12}^0/\chi_{11}^0$, $\bar{E}_2^2 = \chi_{22}^0/\chi_{11}^0$. The z_0 factors appear now in U_{GA} since we want to use the bare χ_0 in Eq. 1. All correlation effects are incorporated in the definition of U_{GA} which therefore can be viewed as a vertex corrected interaction term in the magnetic $p-h$ channel. Note that U_{GA} is not strictly a pure interaction term, but is weighted by kinetic terms which enhance its \mathbf{q} -dependence.

Figure 7 compares χ_{11}^0 , χ_{12}^0 , χ_{22}^0 , and the derived \bar{E}_1 , \bar{E}_2 – the results are fairly insensitive to doping or band parameters. The sharp structures associated with nesting show up only in χ_{11}^0 , while the other χ 's are smooth, and the \bar{E} 's contain only a weak structure imposed from χ_{11}^0 . Hence U_{GA} remains a smooth, weakly varying function of \mathbf{q} , and the instabilities are controlled by the peaks in χ_0 . Figure 8(a) shows how U_{GA} varies as the bare U is increased. At small U , $U_{GA} \rightarrow U$ and the conventional HF+RPA is recovered. Again the results do not depend strongly on doping (Fig. 8(b)) or dispersion. The general trend is that at large U U_{GA} tends to saturate, and the large- \mathbf{q} components of U_{GA} are reduced most strongly, tending to favor instabilities nearer $\Gamma = (0,0)$, suggestive of ferromagnetic domains. Fig. 8 should be compared with Fig. 2 of Vilk and Tremblay¹⁶, who find a similar saturation. Since these authors employ a very different

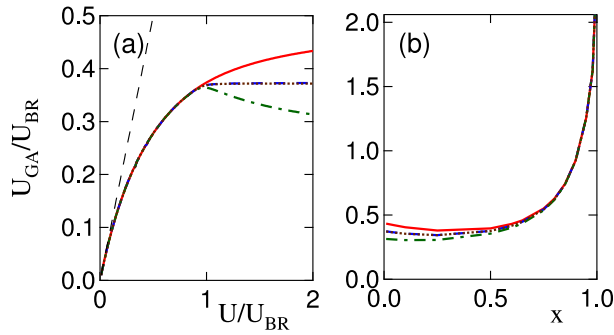


FIG. 8: (Color online.) (a) Variation of U_{GA} with U for $x = 0.01$. (b) Variation of U_{GA} with x for $U = 2U_{BR}$. U_{GA} varies with \mathbf{q} , and the figure shows $\mathbf{q} = \Gamma$ (red solid line), $(\pi, 0)$ (blue dashed line), $(\pi/2, \pi/2)$ (brown dotted line), and (π, π) (green dot-dashed line). The \mathbf{q} -points along the zone diagonal, $(\pi, 0)$ and $(\pi/2, \pi/2)$ have nearly identical behavior.

perscription for including vertex corrections, the similarity of our results gives considerable further confidence to the trends we find. In addition since the Gutzwiller approximation has a simple interpretation in terms of kinetic energy suppression due to correlation our results shed further light on the physical meaning of the vertex corrections.

V. GUTZWILLER MAGNETIC PHASE DIAGRAMS OF THE CUPRATES

Figure 9 shows our main result, the magnetic phase diagrams of LSCO and Bi2201 calculated in the Gutzwiller GA+RPA approach, based on the Stoner criterion, Eq. 1. The phase diagram for Bi2201 is fairly generic, and we have found similar results for NCCO, Bi2212 [neglecting bilayer splitting] and SCOC, while the LSCO phase diagram is limited to the dispersion parameters of LSCO(1). Thus, for electron doping the phase diagram is very simple, dominated by simple AF order with \mathbf{q} very close to (π, π) , while for hole doping there is a competition between the SAF and ANN order, except in LSCO, where SAF order dominates. It is possible that ANN order is relevant to the ‘checkerboard’ phase seen in STM studies of several cuprates, as discussed briefly below.

Results for HF+RPA are similar, but since U_{eff} in Eq. 1 is not bounded ($U_{eff} = U$), there would be magnetic instabilities for all dopings, with transitions to the $(\pi, 0)$ and Γ plateaus, as in Fig. 1. In contrast, in the GA+RPA calculation U_{GA} saturates, and magnetic order exists only in a limited doping range in the cuprates, primarily in the range where the (π, π) plateau exists. However, this doping range encompasses the full doping range of relevance to cuprate physics – including the overdoped regime – if a doping independent $U \sim 6 - 8t$ is assumed. Thus, to have a magnetic quantum critical point near optimal doping, one must go beyond the

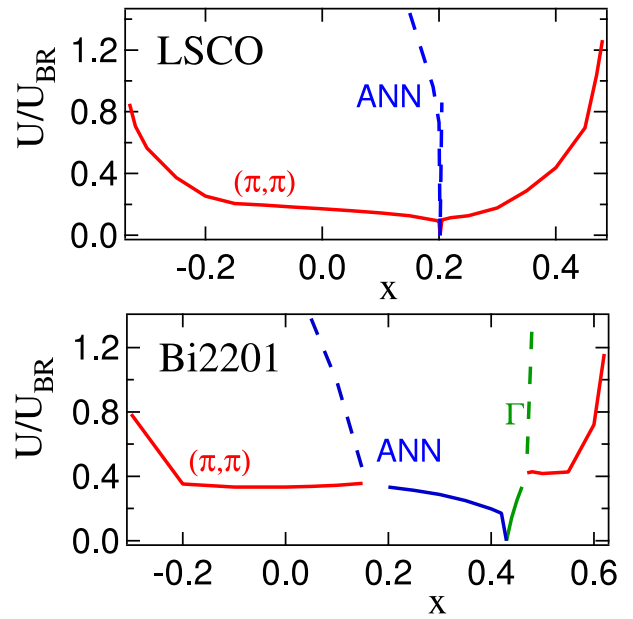


FIG. 9: (Color online.) Gutzwiller magnetic phase diagrams for (a) LSCO(2) and (b) Bi2201(2). Dashed lines indicate metastable states – extensions of the condition $U_{Gutz}\chi = 1$ for one phase beyond the point where another phase has become unstable.

one-band GA+RPA approach. The limited doping range for the magnetic phases has also been seen in a $d = \infty$ study.¹¹ Analogously to HF+RPA, GA+RPA determines the transition line at which the mean field state becomes unstable, but the energies are evaluated at mean field level. Fluctuation contributions to the energy will most likely lower the energy of the paramagnetic (disordered) phase further reducing the stability range of the magnetic phases.

VI. DISCUSSION

There have by now been countless calculations concerning nanoscale phase separation or stripe phases in cuprates, and this is becoming a paradigm in many other correlated electronic systems as well. We believe, however, that the present results are unique in providing a systematic phase diagram, covering the full doping dependence¹² and all possible q -vectors for realistic band dispersions, and indeed finding that the dominant instabilities may be different in different cuprates.

A. Extension to Charge Instabilities

While the above has provided a thorough analysis of possible magnetic instabilities, nothing has been said about competing instabilities in the charge channel –

charge density waves (CDWs) or ‘stripes’. Of course, one possibility is that charge order arises as a secondary effect following the spin order, with $\delta\rho \propto (\delta M)^2$. The case where the charge instability is primary will be somewhat harder to analyze. That is because the corresponding Stoner factor analysis is likely to require an extension beyond the Hubbard model, and hence involve greater uncertainty in the choice of $U_{eff}(\mathbf{q})$. For charge instabilities, the corresponding Stoner denominator is nothing but the (zero frequency) dielectric constant $\epsilon/\epsilon_0 = 1 + V(\mathbf{q})\chi_0(\mathbf{q}, \omega = 0)$, where ϵ_0 is a background dielectric constant and $V(\mathbf{q})$ is a Coulomb potential. When $V(\mathbf{q})$ is taken as either the Hubbard U or a long-range Coulomb interaction,¹⁷ ϵ is always positive and there is no instability.

Moreover, from the theory of dielectric stability, it is known that ϵ cannot fall in the range between 0 and 1 [equivalently $\epsilon^{-1} \leq 1$], and an instability $\epsilon = 0$ must be approached through negative values of ϵ .¹⁸ While a purely electronic instability could still arise via inclusion of local field effects, the most natural situation arises when electron-phonon coupling is included. A simple s wave instability will be suppressed by the on-site Coulomb repulsion as shown in Ref. 10 but one can still have instabilities in other channels. To the extent that the matrix elements which determine the channel have a smooth behavior one will have a Stoner denominator similar to Eq. (1) with $U_{eff}^{(ep)} \sim g^2 D_0 / \epsilon_e \Omega_{ph}^2$, where g is the electron-phonon coupling parameter, D_0 the corresponding bare phonon propagator, Ω_{ph} a bare phonon frequency, and ϵ_e an electron-electron dielectric constant.¹⁰

Thus, since the instability is also controlled by a Stoner factor, the results of the present paper will also apply for charge instabilities. This is consistent with the common expectation that CDWs and spin density waves (SDWs) are controlled by the same nesting instabilities. Stated differently, the Stoner criterion is a formal expression of the idea that $P/K \geq 1$ for an instability, where P , the interaction energy, is represented by U_{eff} while the kinetic energy K is measured via χ_0^{-1} . The kinetic energy is closely tied to the band structure, and carries important material-specific information. In contrast, the potential energy is fairly featureless, leading to smoothly varying $U_{eff}(\mathbf{q})$. Thus, the locations of the instabilities are controlled by peaks in χ_0 , and a \mathbf{q} -dependent U can only shift the dominant instability between two peaks of comparable height. In the remainder of this section, when we discuss comparison to experiment, it will be seen that the present model has correctly determined the dominant \mathbf{q} values, but that in several cases experiment points more toward CDWs than SDWs.

B. Stripes vs Checkerboards

There have been a number of recent hints that the ‘stripe’ order in underdoped $\text{La}_{2-x}\text{A}_x\text{CuO}_{4+\delta}$, $\text{A} = \text{Sr}$ (LSCO) or Ba (LBCO) is not the same phenomenon as

the ‘checkerboard’ order found in $\text{Sr}_2\text{CuO}_2\text{Cl}_2$ (SCOC) and $\text{Bi}_2\text{Sr}_2\text{CaCu}_2\text{O}_8$ (Bi-2212). Thus, resonant soft x-ray scattering experiments find evidence of charge order in LBCO (stripes)¹⁹ but not in $\text{Ca}_2\text{CuO}_2\text{Cl}_2$ (checkerboards)²⁰, while evidence for time reversal symmetry breaking has been found in $\text{YBa}_2\text{Cu}_3\text{O}_{7-\delta}$ (YBCO), but not in LSCO²¹. The present results suggest a connection between the ANN and checkerboard phases, in that the periodicity of the latter also scales with the antinodal nesting vector²², and a further connection between the (π, π) plateau and stripes. Thus it is quite interesting to observe that the ANN phase is virtually absent for the LSCO(2) dispersion, where evidence for conventional stripes is strongest.

C. Conventional and VHS nesting

In 1D systems the susceptibility diverges at $\mathbf{q} = 2\mathbf{k}_F$ at all dopings, due to perfect (flat band) nesting. The present results generalize this to 2D systems: the dominant instability is generally associated with double nesting, but since χ_0 in general does not diverge, a finite coupling U is required to drive an instability. An exception is VHS nesting⁷, for which χ_0 has a logarithmic divergence.

At the VHS, there are two competing instabilities, AF at (π, π) and FM at Γ , corresponding to the magnetic branch of the $SO(8)$ phase diagram of the cuprates, and these are responsible for the commensurate pinning near (π, π) and Γ , respectively.²³ Doped away from the VHS, these instabilities evolve into the two dominant peaks of the susceptibility, and can be considered as ‘generalized VHS nesting’. As such, they dominate the magnetic physics of the cuprates over the full doping range, coextensive with the limits of the (π, π) -plateau in the susceptibility.

D. VHS and FM

Recently, Storey *et al.*²⁴ proposed that the generic behavior of high- T_c cuprates could be understood if the pairing interaction (or pairing energy cutoff) falls off rapidly near the VHS. A recent experiment²⁵ does indeed confirm that x_{opt} scales with T_c , but $x_{opt}/x_{VHS} < 1$. The present results suggest that most cuprates will have strong FM fluctuations near the VHS, which are incompatible with simple d-wave superconductivity. Empirical evidence for FM fluctuations has been noted previously²⁶. While some previous calculations²⁷ have found evidence of ferromagnetism near a VHS, others²⁸ have suggested that FM instabilities were unlikely in competition with incommensurate susceptibility. The present calculations confirm that a dominant FM susceptibility should be present near the VHS.

E. Limitations of Present Approach

1. k_z -dispersion

The advantage of two-dimensional materials is that it is straightforward to display the susceptibility maps and nesting curves. In 3D, the curves become *nesting surfaces* and the susceptibility maps are 4-dimensional. One can speculate that the dominant susceptibility peaks correspond to triple-nesting points. For quasi-2D materials, it should be possible to analyze a series of cuts perpendicular to the (weakly-dispersing) z -axis.

2. Nanoscale phase separation

In principle, the present results could provide information on nanoscale phase separation (NPS) as well. One model of NPS is that there are different instabilities associated with particular dopings [e.g., half filling and the VHS], and that these two phases are more stable than uniform phases at intermediate dopings. In this case, the two end phases could still be described by nesting maps, only at particular dopings. For instance, in the HF+RPA analysis of LSCO(2), the FM phase is stable only very close to the VHS, and could lead to NPS with a second phase at the undoped insulator.

3. Away from the Instability Threshold – Towards Strong Correlations

The Stoner criterion determines which \mathbf{q} value is most unstable, and the minimum U needed to drive that instability. However, as U increases above threshold, the \mathbf{q} of the ordered phase may shift. Thus, at half filling, when a full gap can be formed, \mathbf{q} will no longer be determined by best nesting, but by the largest gap. This tends to favor more commensurate \mathbf{q} values, leading to a pinning of \mathbf{q} at these commensurate values over a wide range of parameters. We find that as U increases, there is a first order transition from an incommensurate phase with Fermi surface pockets to a commensurate $[(\pi, \pi)$ or $(\pi, 0)]$ phase that is fully gapped.³⁴ Away from half filling, Luttinger's theorem ensures the persistence of a Fermi surface, so nesting instabilities should persist over a wider range of U 's.

Furthermore, as we have seen above, the \mathbf{q} -value corresponding to the largest $U_{eff}(\mathbf{q})\chi_0(\mathbf{q})$ can shift with U . Typically, for U_{GA} the shift is to a smaller \mathbf{q} -value, associated with an instability towards FM order (in the magnetic channel) or NPS (in the charge channel).

VII. CONCLUSION

The present results provide a constructive scheme for identifying the dominant nesting instabilities for any two

TABLE I: I. Band Parameter Sets

Parameter	NCCO	Bi-2201(1)	Bi-2201(2)	LSCO(1)	LSCO(2)
t	420	250	435	195.6	419.5
t'	-100	-55	-120	-18.5	-37.5
t''	65	27.5	40	15.7	18
t'''	7.5	0	0	17.5	34
t''''	0	0	0	4.35	0
Z	0.5	1	0.5	1	0.5
Ref.:	4	29	30	31	4

dimensional material. Clearly, for Fermi surfaces with multiple sections, a large number of nesting curves are possible, leading to extremely complicated susceptibility maps. Nevertheless, the present scheme will automatically sort out the possible double nesting peaks and follow their evolution with doping. This should allow a much more detailed understanding of 2D phase diagrams, particularly for magnetic phases, where the interaction U has negligible \mathbf{q} -dependence.

The good agreement of the GA+RPA calculations with more detailed variational calculations at half filling³⁴ and with exact and numerical results in $d = \infty$,¹¹ and of the AF+SC model in electron doped cuprates with experiments gives us confidence in the model. Accordingly, we note the following three points. First, within GA+RPA, the paramagnetic state is unstable over the full hole-doping range in the cuprates, including overdoped. To avoid this conclusion, and restore a Fermi liquid phase in the overdoped regime, it may be necessary to include non Gaussian fluctuations³⁵ or an additional doping dependence for U . The origin of any such doping dependence lies outside the GA treatment of the Hubbard model. Second, the (π, π) phase, or its incommensurate extension, is unstable against a competing ANN order in [most] hole-doped cuprates. Third, there is a material dependence to the phase diagram, and LSCO may have a very different doping dependence than other cuprates.

The results have been applied to a number of model dispersions for the cuprates. A possible pseudogap candidate has been identified and a distinction between stripes and checkerboards proposed. These findings will be discussed in greater detail in ensuing publications.

This work is supported by the US Department of Energy, Office of Science, Basic Energy Sciences contract DE-FG02-07ER46352, and benefited from the allocation of supercomputer time at NERSC, Northeastern University's Advanced Scientific Computation Center (ASCC). RSM's work has been partially funded by the Marie Curie Grant PIF-GA-2008-220790 SOQCS, while GS' work is supported by the Vigoni Program 2007-2008 of the Ateneo Italo-Tedesco Deutsch-Italienisches Hochschulzentrum.

Appendix A: Notes to Table I: Band Parameters

In Table I, all hopping parameters are given in meV. The t'''' term for LSCO(1) is the coefficient of a term $c_x(2a)c_y(2a)$ in Eq. 3. NCCO, LSCO(2), and Bi2201(2) data sets are fit to LDA band dispersions of the near-Fermi level antibonding CuO_2 band, and are appropriate for the Gutzwiller analysis. The data sets LSCO(1) and Bi2201(1) are taken from fits to experimental ARPES data. To the extent that the bands are renormalized by a \mathbf{q} -independent factor Z , the effective bare susceptibilities $Z\chi$ can be used in the Gutzwiller analysis, while χ_{0M} occurs at the same \mathbf{q} .

Recently it has been suggested that the enhanced nesting, such as observed in LSCO(1), may be associated with stripe formation³².

Appendix B: Gutzwiller plus random-phase approximation formalism.

Here we sketch the GA+RPA formalism and define the relevant quantities. For a review see Ref. 36.

The susceptibility can be computed in the longitudinal¹⁰ or in the transverse channel.³⁷ As

shown bellow both results are equivalent as dictated by spin rotational invariance on a paramagnetic (singlet) ground state.

For later use we define the density matrix associated with the unprojected Slater determinant, $|\phi\rangle$, as

$$\rho_{ij}^{\sigma\sigma'} \equiv \langle \phi | c_{j\sigma'}^\dagger c_{i\sigma} | \phi \rangle$$

and as a shorthand we define $\rho_{ij\sigma} \equiv \rho_{ij}^{\sigma\sigma}$.

We start from the spin-rotational invariant Gutzwiller energy functional for the Hubbard model defined in terms of $\rho_{ij}^{\sigma\sigma'}$ and the double occupancy in the Gutzwiller variational state D_i . As derived e.g. in Ref. 37 the functional reads,

$$E^{GA} = \sum_{i,j} t_{ij} \langle \phi | \Psi_i^\dagger \mathbf{z}_i \mathbf{z}_j \Psi_j | \phi \rangle + U \sum_i D_i.$$

where we have defined the spinor operators

$$\Psi_i^\dagger = (c_{i\uparrow}^\dagger, c_{i\downarrow}^\dagger) \quad \Psi_i = \begin{pmatrix} c_{i\uparrow} \\ c_{i\downarrow} \end{pmatrix}$$

and the \mathbf{z} -matrix

$$\mathbf{z}_i = \begin{pmatrix} z_{i\uparrow} \cos^2 \frac{\varphi_i}{2} + z_{i\downarrow} \sin^2 \frac{\varphi_i}{2} & \frac{S_i^-}{2S_i^z} [z_{i\uparrow} - z_{i\downarrow}] \cos \varphi_i \\ \frac{S_i^+}{2S_i^z} [z_{i\uparrow} - z_{i\downarrow}] \cos \varphi_i & z_{i\uparrow} \sin^2 \frac{\varphi_i}{2} + z_{i\downarrow} \cos^2 \frac{\varphi_i}{2} \end{pmatrix}$$

$$\tan^2 \varphi_i = \frac{S_i^+ S_i^-}{(S_i^z)^2}.$$

with the z factors given by

$$z_{i\sigma} = \frac{\sqrt{(1 - \rho_{ii} + D_i)(\frac{1}{2}\rho_{ii} + \frac{S_i^z}{\cos(\varphi_i)} - D_i)} + \sqrt{D_i(\frac{1}{2}\rho_{ii} - \frac{S_i^z}{\cos(\varphi_i)} - D_i)}}{\sqrt{(\frac{1}{2}\rho_{ii} + \frac{S_i^z}{\cos(\varphi_i)})(1 - \frac{1}{2}\rho_{ii} - \frac{S_i^z}{\cos(\varphi_i)})}}$$

and for clarity spin expectation values are denoted by $S_i^+ = \rho_{ii}^{\uparrow,\downarrow}$, $S_i^- = \rho_{ii}^{\downarrow,\uparrow}$, $S_i^z = (\rho_{ii}^{\uparrow,\uparrow} - \rho_{ii}^{\downarrow,\downarrow})/2$, and $\rho_{ii} = \rho_{ii}^{\uparrow,\uparrow} + \rho_{ii}^{\downarrow,\downarrow}$.

In the limit of a vanishing rotation angle φ the \mathbf{z} -matrix becomes diagonal and the renormalization factors reduce to those of the standard Gutzwiller approximation.

For a homogeneous, paramagnetic system ($z_{i\sigma} \equiv z_0$, $\varphi_i = 0$) the expansion of the Gutzwiller energy functional up to second order in the particle-hole excitations reads,

$$\delta E^{GA} = \delta E^{ff} + \delta E_c^{GA} + \delta E_{lo}^{GA} + \delta E_{tr}^{GA} \quad (\text{B1})$$

The first contribution is the free fermion part,

$$\delta E^{ff} = \sum_{k > k_F, k' < k_F; \sigma, \sigma'} (\epsilon_{\mathbf{k}} - \epsilon_{\mathbf{k}'}) \delta \rho_{\mathbf{k}\mathbf{k}'}^{\sigma\sigma'} \delta \rho_{\mathbf{k}'\mathbf{k}}^{\sigma'\sigma}.$$

$\epsilon_{\mathbf{k}}$ denotes the dispersion of the Gutzwiller quasiparticles whereas $\epsilon_{\mathbf{k}}^0$ corresponds to the unrenormalized dispersions, i.e. $\epsilon_{\mathbf{k}} = z_0^2 \epsilon_{\mathbf{k}}^0$.

The remaining part in Eq. (B1) is due to quasiparticle interactions and separates into contributions from the charge (c), the longitudinal (lo) and transverse (tr) spin channel. δE_c^{GA} and δE_{lo}^{GA} have been derived in detail in Ref. 10.

For our purposes we report in the following the expansion in the longitudinal channel:

$$\delta E_{lo}^{GA} = \frac{1}{2N} \sum_{\mathbf{q}} \begin{pmatrix} \delta S_{\mathbf{q}}^z \\ \delta T_{\mathbf{q}}^z \end{pmatrix} V_q^{zz} \begin{pmatrix} \delta S_{-\mathbf{q}}^z \\ \delta T_{-\mathbf{q}}^z \end{pmatrix} \quad (\text{B2})$$

$$\underline{\underline{V_q^{zz}}} = \begin{pmatrix} 2N_{\mathbf{q}} & 2z_0 z'_t \\ 2z_0 z'_t & 0 \end{pmatrix} \quad (\text{B3})$$

and in the transverse magnetic channel which has been derived in Ref. 37

$$\delta E_{tr}^{GA} = \frac{1}{N} \sum_{\mathbf{q}} \begin{pmatrix} \delta S_{\mathbf{q}}^+ \\ \delta T_{\mathbf{q}}^+ \end{pmatrix} \underline{\underline{V_q^{+-}}} \begin{pmatrix} \delta S_{-\mathbf{q}}^- \\ \delta T_{-\mathbf{q}}^- \end{pmatrix} \quad (\text{B4})$$

$$\underline{\underline{V_q^{+-}}} = \begin{pmatrix} N_{\mathbf{q}} & z_0 z'_t \\ z_0 z'_t & 0 \end{pmatrix}. \quad (\text{B5})$$

The relevant fluctuations have been defined as

$$\begin{aligned} \delta S_q^z &= \frac{1}{2} \sum_{k\sigma} \sigma \delta \rho_{k+q,k}^{\sigma,\sigma}, \\ \delta T_q^z &= \frac{1}{2} \sum_{k\sigma} \sigma (\varepsilon_{k+q}^0 + \varepsilon_k^0) \delta \rho_{k+q,k}^{\sigma,\sigma}, \\ \delta S_q^\sigma &= \sum_k \delta \rho_{k+q,k}^{\sigma,-\sigma}, \\ \delta T_q^\sigma &= \sum_k (\varepsilon_{k+q}^0 + \varepsilon_k^0) \delta \rho_{k+q,k}^{\sigma,-\sigma}. \end{aligned}$$

The 11 element of the interaction kernel is given by

$$N_{\mathbf{q}} = (z'_t)^2 N_{1\mathbf{q}} + 2z_0 z'_t e_0 \quad (\text{B6})$$

with

$$e_0 \equiv \frac{1}{N} \sum_{\mathbf{k}\sigma} \epsilon_{\mathbf{k}\sigma}^0 n_{\mathbf{k}\sigma} = U_{BR}/8. \quad (\text{B7})$$

Here U_{BR} is the Brinkman-Rice energy. N_1 is similar, but requires separate averages for different components of the energy:

$$\begin{aligned} N_{1\mathbf{q}} &= \frac{1}{N} \sum_{\mathbf{k}\sigma} \epsilon_{\mathbf{k}+\mathbf{q}\sigma}^0 n_{\mathbf{k}\sigma} \\ &= -t[c_{qx} + c_{qy}] \langle c_{kx} + c_{ky} \rangle - 4t' c_{qx} c_{qy} \langle c_{kx} c_{ky} \rangle \\ &\quad - t''[c_{2qx} + c_{2qy}] \langle c_{2kx} + c_{2ky} \rangle \\ &\quad - 2t'''[c_{qx} c_{2qy} + c_{qy} c_{2qx}] \langle c_{kx} c_{2ky} + c_{ky} c_{2kx} \rangle, \end{aligned} \quad (\text{B8})$$

in an obvious notation.

Furtheron we define the susceptibility matrices for the bare time-ordered correlation functions both in the longitudinal

$$\chi_q^{0,lo}(t) = \frac{-i}{N} \begin{pmatrix} \langle \mathcal{T} \hat{S}_q^z(t) \hat{S}_{-q}^z(0) \rangle_0 & \langle \mathcal{T} \hat{S}_q^z(t) \hat{T}_{-q}^z(0) \rangle_0 \\ \langle \mathcal{T} \hat{T}_q^z(t) \hat{S}_{-q}^z(0) \rangle_0 & \langle \mathcal{T} \hat{T}_q^z(t) \hat{T}_{-q}^z(0) \rangle_0 \end{pmatrix},$$

and in the transverse channel

$$\chi_q^{0,tr}(t) = \frac{-i}{N} \begin{pmatrix} \langle \mathcal{T} \hat{S}_q^+(t) \hat{S}_{-q}^-(0) \rangle_0 & \langle \mathcal{T} \hat{S}_q^+(t) \hat{T}_{-q}^-(0) \rangle_0 \\ \langle \mathcal{T} \hat{T}_q^+(t) \hat{S}_{-q}^-(0) \rangle_0 & \langle \mathcal{T} \hat{T}_q^+(t) \hat{T}_{-q}^-(0) \rangle_0 \end{pmatrix},$$

where a hat has been added to distinguish fluctuations (δS_q^+) from operators (\hat{S}_q^+).

The longitudinal susceptibility describes the $\Delta m_z = 0$, singlet to triplet excitations of the paramagnetic state while the transverse describes $\Delta m_z = \pm 1$ spin excitations. Spin rotational invariance dictates that these excitations should be degenerate.

One obtains for these correlation functions

$$\chi_{\mathbf{q}}^{0,lo} = \frac{1}{4N} \sum_{\mathbf{k}\sigma} \begin{pmatrix} 1 & \epsilon_{\mathbf{k}}^0 + \epsilon_{\mathbf{k}+\mathbf{q}}^0 \\ \epsilon_{\mathbf{k}}^0 + \epsilon_{\mathbf{k}+\mathbf{q}}^0 & (\epsilon_{\mathbf{k}}^0 + \epsilon_{\mathbf{k}+\mathbf{q}}^0)^2 \end{pmatrix} \frac{n_{\mathbf{k}+\mathbf{q},\sigma} - n_{\mathbf{k}\sigma}}{\omega + \epsilon_{\mathbf{k}+\mathbf{q}} - \epsilon_{\mathbf{k}}}$$

and

$$\chi_{\mathbf{q}}^{0,tr} = \frac{1}{N} \sum_{\mathbf{k}} \begin{pmatrix} 1 & \epsilon_{\mathbf{k}}^0 + \epsilon_{\mathbf{k}+\mathbf{q}}^0 \\ \epsilon_{\mathbf{k}}^0 + \epsilon_{\mathbf{k}+\mathbf{q}}^0 & (\epsilon_{\mathbf{k}}^0 + \epsilon_{\mathbf{k}+\mathbf{q}}^0)^2 \end{pmatrix} \frac{n_{\mathbf{k}+\mathbf{q},\uparrow} - n_{\mathbf{k},\downarrow}}{\omega + \epsilon_{\mathbf{k}+\mathbf{q}} - \epsilon_{\mathbf{k}}}.$$

For the non-interacting Gutzwiller quasiparticles spin-rotational invariance is thus guaranteed from the relation

$$\chi_{\mathbf{q}}^{0,lo} = \frac{1}{2} \chi_{\mathbf{q}}^{0,tr} \quad (\text{B9})$$

This identity is preserved within the GA+RPA when we compute the interacting susceptibilities from the RPA series

$$\begin{aligned} \chi_{\mathbf{q}}^{lo} &= \chi_{\mathbf{q}}^{0,lo} - \chi_{\mathbf{q}}^{0,lo} V_{\mathbf{q}}^{zz} \chi_{\mathbf{q}}^{lo} \\ \chi_{\mathbf{q}}^{tr} &= \chi_{\mathbf{q}}^{0,tr} - \chi_{\mathbf{q}}^{0,tr} V_{\mathbf{q}}^{+-} \chi_{\mathbf{q}}^{tr} \end{aligned}$$

since from Eqs. (B3, B5) the interaction kernels are related by $V^{zz} = 2V^{tr}$. Clearly the energies of particle hole excitations described by these equations are degenerate. In particular they lead to the same Stoner criteria in both channels.

Appendix C: Derivatives of the Gutzwiller approximation z factors

The expressions involve the following derivatives of $z_{i\sigma}$ in the longitudinal channel

$$z' \equiv \frac{\partial z_{i\sigma}}{\partial \rho_{ii\sigma}}, \quad (\text{C1})$$

$$z'_{+-} \equiv \frac{\partial z_{i\sigma}}{\partial \rho_{ii-\sigma}}, \quad (\text{C2})$$

$$z''_{++} \equiv \frac{\partial^2 z_{i\sigma}}{\partial \rho_{ii\sigma}^2}, \quad (\text{C3})$$

$$z''_{+-} \equiv \frac{\partial^2 z_{i\sigma}}{\partial \rho_{ii\sigma} \partial \rho_{ii-\sigma}}, \quad (\text{C4})$$

$$z''_{--} \equiv \frac{\partial^2 z_{i\sigma}}{\partial \rho_{ii-\sigma}^2}. \quad (\text{C5})$$

The derivatives in the transverse channel can be related to those in the longitudinal channel as follows,

$$z'_t \equiv \frac{\partial z_{i,\sigma,-\sigma}}{\partial \rho_{ii}^{\sigma,-\sigma}} = z' - z'_{+-} = \frac{2\delta}{1-\delta^2} \left(\frac{1}{z_0} - z_0 \right),$$

$$z''_t \equiv \frac{\partial^2 z_{i,\sigma\sigma}}{\partial \rho_{ii}^{\sigma,-\sigma} \partial \rho_{ii}^{\sigma,-\sigma}} = \frac{1}{2} (z''_{++} + 2z''_{+-} + z''_{--})$$

$$= \frac{2z_0}{(1-\delta^2)^2} \left\{ 1 - 2\delta^2 \left(\frac{1}{z_0^2} - 1 \right) \right\}$$

$$-\frac{1}{2} \frac{z_0}{(1-\delta-2D)^2}.$$

On the right we have given explicit expressions in terms of δ , the doping measured with respect to half-filling and the double occupancy D in the paramagnetic state.

-
- ¹ A. Macridin, M. Jarrell, T. Maier, and D.J. Scalapino, Phys. Rev. Lett. **99**, 237001 (2007).
 - ² R.S. Markiewicz, S. Sahrakorpi, and A. Bansil, Phys. Rev. B **76**, 174514 (2007).
 - ³ F. Ronning, K.M. Shen, N.P. Armitage, A. Damascelli, D.H. Lu, Z.-X. Shen, L.L. Miller, and C. Kim, Phys. Rev. B **71**, 094518 (2005); J. Graf, G.-H. Gweon, K. McElroy, S.Y. Zhou, C. Jozwiak, E. Rotenberg, A. Bill, T. Sasagawa, H. Eisaki, S. Uchida, H. Takagi, D.-H. Lee, and A. Lanzara, Phys. Rev. Lett. **98**, 067004 (2007).
 - ⁴ R.S. Markiewicz, S. Sahrakorpi, M. Lindroos, Hsin Lin, and A. Bansil Phys. Rev. B **72**, 054519 (2005).
 - ⁵ A.A. Aligia, Phys. Rev. B **39**, 6700 (1989); Q. Si, Y. Zha, K. Levin, and J.P. Lu, Phys. Rev. B **47**, 9055 (1993); P. Bénard, L. Chen, and A.-M.S. Tremblay, Phys. Rev. B **47**, 15217 (1993); M. Lavagna and G. Stemann, Phys. Rev. B **49**, 4235 (1994); F. Onufrieva and P. Pfeuty, Phys. Rev. B **61**, 799 (2000); M.R. Norman, Phys. Rev. B **61**, 14751 (2000).
 - ⁶ For an example of this extended commensurate nesting, see frames j, k of Fig. 5.
 - ⁷ T.M. Rice and G.K. Scott, Phys. Rev. Lett. **35**, 120 (1975).
 - ⁸ R. Hlubina and T.M. Rice, Phys. Rev. B **51**, 9253 (1995).
 - ⁹ O.K. Andersen, O. Jepsen, A.I. Liechtenstein, and I.I. Mazin, Phys. Rev. B **49**, 4145 (1994).
 - ¹⁰ A. DiCiolo, J. Lorenzana, M. Grilli, and G. Seibold, Phys. Rev. B **79**, 085101 (2009).
 - ¹¹ F. Günther, G. Seibold, and J. Lorenzana, Phys. Rev. Lett. **98**, 176404 (2007).
 - ¹² Some previous determinations of stripe incommensurability vs doping, but for a limited range of q -values, are: J. Lorenzana and G. Seibold, Phys. Rev. Lett. **89**, 136401 (2002); G. Seibold and J. Lorenzana, Phys. Rev. B **69**, 134513 (2004).
 - ¹³ F. Gebhard, Phys. Rev. B **41**, 9452 (1990).
 - ¹⁴ G. Kotliar and A.E. Ruckenstein, Phys. Rev. Lett. **57**, 1362 (1986).
 - ¹⁵ D. Vollhardt, Rev. Mod. Phys. **56**, 99 (1984).
 - ¹⁶ Y.M. Vilks and A.-M.S. Tremblay, J. Phys. I **7**, 1309 (1997).
 - ¹⁷ R.S. Markiewicz and A. Bansil, Phys. Rev. B **75**, 020508(R) (2007).
 - ¹⁸ O.V. Dolgov, D.A. Kirzhnits, and E.G. Maksimov, Rev. Mod. Phys. **53**, 81 (1981).
 - ¹⁹ P. Abbamonte, A. Rusydi, S. Smadici, G.D. Gu, G.A. Sawatzky, and D.L. Feng, Nature Phys. **1**, 155 (2005).
 - ²⁰ S. Smadici, P. Abbamonte, M. Taguchi, Y. Kohsaka, T. Sasagawa, M. Azuma, M. Takano, and H. Takagi, Phys. Rev. B **75**, 075104 (2007).
 - ²¹ G.J. MacDougall, A.A. Aczel, J.P. Carlo, T. Ito, J. Rodriguez, P.L. Russo, Y.J. Uemura, S. Wakimoto, G.M. Luke, Phys. Rev. Lett. **101**, 017001 (2008).
 - ²² K.M. Shen, F. Ronning, D.H. Lu, F. Baumberger, N.J.C. Ingle, W.S. Lee, W. Meevasana, Y. Kohsaka, M. Azuma, M. Takano, H. Takagi, and Z.-X. Shen, Science **307**, 901 (2005); W.D. Wise, M.C. Boyer, K. Chatterjee, T. Kondo, T. Takeuchi, H. Ikuta, Y. Wang, and E.W. Hudson, Nature Physics **4**, 696 (2008).
 - ²³ R.S. Markiewicz and M.T. Vaughn, Phys. Rev. B **57**, R14052 (1998).
 - ²⁴ J.G. Storey, J.L. Tallon, and G.V.M. Williams, Phys. Rev. B **76**, 174522 (2007).
 - ²⁵ A.D. Palczewski, T. Kondo, R. Khasanov, N.N. Kolesnikov, A.V. Timonina, E. Rotenberg, T. Ohta, A. Bendounan, Y. Sassa, A.V. Fedorov, S. Pailh  s, A.F. Santander-Syro, J. Chang, M. Shi, J. Mesot, H.M. Fretwell, and A. Kaminski, Phys. Rev. B **78**, 054523 (2008).
 - ²⁶ A. Kopp, A. Ghosal, and S. Chakravarty, Proc. Natl. Acad. Sci. USA **104**, 6123 (2007).
 - ²⁷ R. Hlubina, S. Sorella, and F. Guinea, Phys. Rev. Lett. **78**, 1343 (1997); R. Hlubina, Phys. Rev. B **59**, 9600 (1999); D. Vollhardt, N. Bl  mer, K. Held, M. Kollar, J. Schlipf, and M. Ulmke, Z. Phys. B **103**, 283 (1997); B. Valenzuela, M.A.H. Vozmediano, and F. Guinea, Phys. Rev. B **62**, 11312 (2000).
 - ²⁸ P.A. Igoshev, A.A. Katanin, and V.Yu. Irkhin, J.E.T.P., to be published, (extended version: arXiv:0709.3219).
 - ²⁹ M. Hashimoto, T. Yoshida, H. Yagi, M. Takizawa, A. Fujimori, M. Kubota, K. Ono, K. Tanaka, D.H. Lu, Z.-X. Shen, S. Ono, and Yoichi Ando, Phys. Rev. B **77**, 094516 (2008).
 - ³⁰ We thank Tanmoy Das for providing us with these values, based on LDA.
 - ³¹ M.R. Norman, Phys. Rev. B **75**, 184514 (2007).
 - ³² V.B. Zabolotnyy, A.A. Kordyuk, D.S. Inosov, D.V. Evtushinsky, R. Schuster, B. Buechner, N. Wizen, G. Behr, Sunseong Pyon, H. Takagi, R. Follath, S.V. Borisenko, Europhys. Lett. **86**, 47005 (2009).
 - ³³ R.S. Markiewicz, Phys. Rev. B **70**, 174518 (2004).
 - ³⁴ R.S. Markiewicz, J. Lorenzana, and G. Seibold, unpublished.
 - ³⁵ S. Andergassen, S. Caprara, C. Di Castro, and M. Grilli, Phys. Rev. Lett. **87**, 056401 (2001).
 - ³⁶ J. Lorenzana and G. Seibold, Low. Temp. Physics **32**, 320 (2006).
 - ³⁷ G. Seibold, F. Becca, P. Rubin, and J. Lorenzana, Phys. Rev. B **69**, 155113 (2004).